

## Semimetal-to-semiconductor transition and charge-density-wave suppression in $1T$ -TiSe<sub>2-x</sub>S<sub>x</sub> single crystals

M.-L. Mottas,<sup>1,\*</sup> T. Jaouen,<sup>1,†</sup> B. Hildebrand,<sup>1</sup> M. Rumo,<sup>1</sup> F. Vanini,<sup>1</sup> E. Razzoli,<sup>2,3</sup> E. Giannini,<sup>4</sup>  
C. Barreteau,<sup>4</sup> D. R. Bowler,<sup>5</sup> C. Monney,<sup>1</sup> H. Beck,<sup>1</sup> and P. Aebi<sup>1</sup>

<sup>1</sup>*Département de Physique, Fribourg Center for Nanomaterials, Université de Fribourg, CH-1700 Fribourg, Switzerland*

<sup>2</sup>*Quantum Matter Institute, University of British Columbia, Vancouver, British Columbia, Canada V6T 1Z4*

<sup>3</sup>*Department of Physics and Astronomy, University of British Columbia, Vancouver, British Columbia, Canada V6T 1Z1*

<sup>4</sup>*Department of Quantum Matter Physics, University of Geneva, 24 Quai Ernest-Ansermet, 1211 Geneva 4, Switzerland*

<sup>5</sup>*Department of Physics and Astronomy, London Centre for Nanotechnology, University College London, London WC1E 6BT, United Kingdom*



(Received 5 December 2018; revised manuscript received 20 March 2019; published 1 April 2019)

The transition-metal dichalcogenide  $1T$ -TiSe<sub>2</sub> is a quasi-two-dimensional layered material with a phase transition towards a commensurate charge-density wave (CDW) at a critical temperature  $T_c \approx 200$  K. The relationship between the origin of the CDW instability and the semimetallic or semiconducting character of the normal state, i.e., with the nonreconstructed Fermi-surface topology, remains elusive. By combining angle-resolved photoemission spectroscopy (ARPES), scanning tunneling microscopy (STM), and density functional theory (DFT) calculations, we investigate  $1T$ -TiSe<sub>2-x</sub>S<sub>x</sub> single crystals. Using STM, we first show that the long-range phase-coherent CDW state is stable against S substitutions with concentrations, at least, up to  $x = 0.34$ . The ARPES measurements then reveal a slow but continuous decrease in the overlap between the electron and the hole ( $e$ - $h$ ) bands of the semimetallic normal state well reproduced by DFT and related to slight reductions of both the CDW order parameter and  $T_c$ . Our DFT calculations further predict a semimetal-to-semiconductor transition of the normal state at a higher critical S concentration of  $x_c = 0.9 \pm 0.1$  that coincides with a suppressed CDW state in TiSeS as measured with STM. Finally, we rationalize the  $x$  dependence of the  $e$ - $h$  band overlap in terms of isovalent substitution-induced competing chemical pressure and charge localization effects. Our study highlights the key role of the  $e$ - $h$  band overlap for the CDW instability.

DOI: [10.1103/PhysRevB.99.155103](https://doi.org/10.1103/PhysRevB.99.155103)

### I. INTRODUCTION

Quasi-two-dimensional transition-metal dichalcogenides (TMDCs) are layered compounds exhibiting a wide variety of interesting electronic properties [1], often undergoing charge-density wave (CDW) transitions [2], or/and hosting low-temperature (LT) superconductivity [3] upon electronic doping or pressure (mechanical or chemical as induced by isovalent substitution) [4]. The TMDC  $1T$ -TiSe<sub>2</sub> is one of these materials which has been studied for decades. It undergoes a  $2 \times 2 \times 2$  charge-density modulation with a weak periodic lattice distortion (PLD) occurring around  $T_c \approx 200$  K [5,6]. It is superconducting upon electrical gating [7], Cu intercalation [8], or under pressure [9]. Increasing the crystal-growth temperature further induces Ti self-doping which strongly perturbs the CDW phase coherence [10,11] and drastically decreases the anomalous peak in the temperature-dependent resistivity curves [5].

In contrast to  $1T$ -TiSe<sub>2</sub>, no phase transition has been reported in  $1T$ -TiS<sub>2</sub> [12–14]. It is therefore expected to observe a gradual suppression of the CDW in the ternary compound  $1T$ -TiSe<sub>2-x</sub>S<sub>x</sub> for increasing  $x$ . Studies of  $1T$ -TiSe<sub>2-x</sub>S<sub>x</sub> have already been carried out, mainly based on

temperature-dependent resistivity measurements [5,15–17], but also with Raman scattering [18], tunneling spectroscopy [16], and angle-resolved photoemission spectroscopy (ARPES) [17]. All these investigations concluded that the S substitution monotonically lowers  $T_c$  until a critical concentration  $x_c$  close to 1.

Here, we re-investigate the CDW suppression in  $1T$ -TiSe<sub>2-x</sub>S<sub>x</sub> single crystals by combining ARPES, scanning tunneling microscopy (STM), and density functional theory (DFT) calculations thereby giving a direct view of both real-space and electronic band structures and characterizing the crystals extremely well with respect to native defects and S concentrations. We demonstrate that, in contrast to the electron-donors Ti and Cu intercalants that shift the  $1T$ -TiSe<sub>2</sub> chemical potential [19,20], isovalent S substitutions reduce the electron-hole ( $e$ - $h$ ) band overlap in the normal state and only slightly affect the long-range phase-coherent CDW state as long as the  $1T$ -TiSe<sub>2</sub> normal state remains semimetallic. Our DFT analysis reveals that whereas the isovalent S substitution induces an increase in the overlap of the Ti  $3d$  electron and the Se  $4p$  hole bands by positive chemical pressure, charge localization effects as introduced by the more localized S  $3p$  orbitals leads to a reduced  $p$ - $d$  hybridization. The charge localization effect dominates the structural counterpart of the S substitution and drives the  $e$ - $h$  band-gap opening. The CDW is experimentally

\*Corresponding author: marie-laure.mottas@unifr.ch

†Corresponding author: thomas.jaouen@unifr.ch

found to be removed at  $x \sim 1$  in good agreement with the DFT-predicted semimetal-to-semiconductor transition, therefore demonstrating that the Fermi surface has to host electron and hole pockets for driving the CDW instability.

## II. EXPERIMENTAL DETAILS

The  $1T$ -TiSe $_{2-x}$ S $_x$  single crystals were grown by iodine vapor transport and contain less than 0.2% of intercalated Ti as measured by STM. Constant current STM images were recorded at 4.5 K with an Omicron LT-STM in constant current mode by applying a bias voltage  $V_{\text{bias}}$  to the sample. The base pressure was better than  $5 \times 10^{-11}$  mbars. The temperature-dependent ARPES study was carried out using a Scienta DA30 photoelectron analyzer and monochromatized He-I radiation as an exciting source ( $h\nu = 21.22$ -eV, SPECS UVLS with a TMM 304 monochromator). The total energy resolution was on the order of 12 meV, and the sample temperatures were deduced from fits of the Fermi edge spectra on the Cu sample holder.

## III. COMPUTATIONAL METHOD

DFT model calculations were performed using the plane-wave pseudopotential code VASP [21,22], version 5.3.3. Projector augmented waves [23] were used with the Perdew-Burke-Ernzerhof [24] exchange-correlation functional. The cell size of our model was  $28.035 \times 28.035 \text{ \AA}^2$ . The  $1T$ -TiSe $_2$  surface was modeled with two layers and the bottom Se layer fixed. A Monkhorst-Pack mesh with  $2 \times 2 \times 1$   $k$  points was used to sample the Brillouin zone of the cell. The parameters gave an energy difference convergence of better than 0.01 eV. During structural relaxations, a tolerance of 0.03 eV/Å was applied. STM images were generated using the Tersoff-Hamann [25] approach in which the current  $I(V)$  measured in STM is proportional to the integrated local density of states of the surface using the BSKAN code [26].

In order to compute the electronic band structures measured in ARPES, DFT calculations were performed using the WIEN2K package [27] with the modified Becke-Johnson (mBJ) exchange-correlation potential [28]. This functional contains a tuning parameter  $c_{\text{mBJ}}$  (see Ref. [29]) which has been set to 1.34 to give the best agreement to the measured room-temperature (RT)  $1T$ -TiSe $_2$  pristine band structure. We used a  $2 \times 2 \times 2$  superstructure of eight unit cells of  $1T$ -TiSe $_2$  with in-plane and out-of-plane experimental lattice parameters  $a = 3.54$  and  $c = 6.01 \text{ \AA}$  [5], respectively. By replacing one to four Se atoms with S, we obtained S concentrations of  $x = 0.125, 0.25, 0.375,$  and  $0.5$ , respectively. The associated unit-cell parameters were set to  $a = 3.53, 3.52, 3.51,$  and  $3.50 \text{ \AA}$  and  $c = 5.99, 5.97, 5.95,$  and  $5.93 \text{ \AA}$ , respectively [16]. The calculated band structures were unfolded using the FOLD2BLOCH package [30].

## IV. RESULTS AND DISCUSSION

Figures 1(a) and 1(b) show STM images recorded at +0.6 V and  $T = 4.5$  K. At this  $V_{\text{bias}}$ , the  $2 \times 2$  electronic modulation is not resolved because the CDW phase transition mainly affects the  $1T$ -TiSe $_2$  density of states close to the

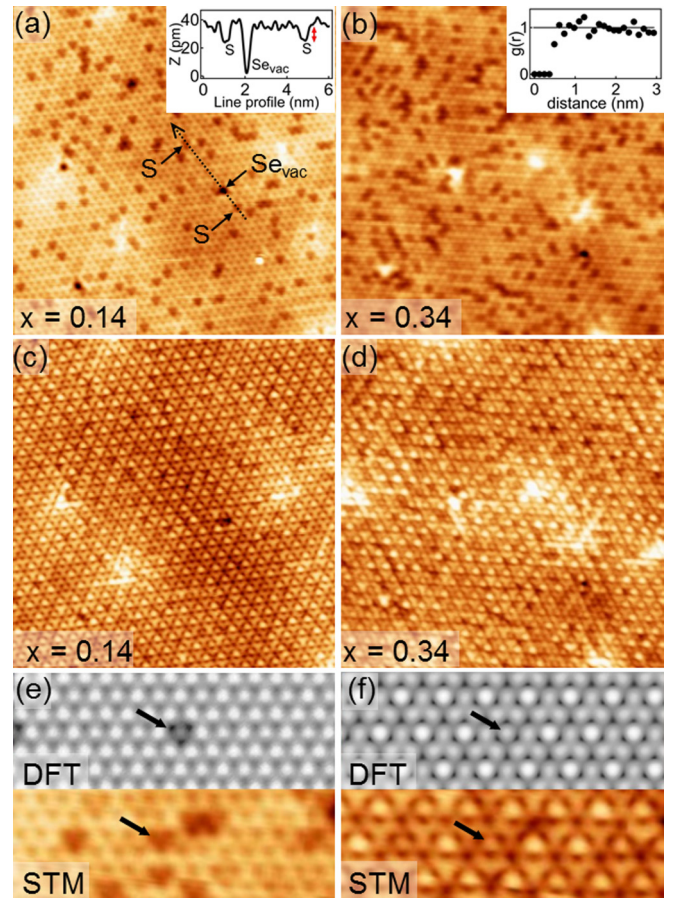


FIG. 1. Constant current ( $I = 0.15$  nA) STM images of  $1T$ -TiSe $_{2-x}$ S $_x$  recorded at  $T = 4.5$  K ( $15 \times 15 \text{ nm}^2$ ). Applied bias voltage is  $V_{\text{bias}} = +0.6$  V for (a) and (b). The insets show a line profile from image (a) and the normalized radial distribution function  $g(r)$  of sulfur atoms from image (b). (c) and (d) Same surface regions as (a) and (b) with  $V_{\text{bias}} = +0.15$  V in order to highlight the  $2 \times 2$  charge-density modulation. (e) and (f) Comparison of DFT-simulated and experimental  $5 \times 3$ -nm $^2$  STM images with sulfur substitutions for  $V_{\text{bias}} = +0.6$  V (e) and  $V_{\text{bias}} = +0.1$  V (DFT) and  $+0.15$  V (STM) (f). The arrows on (e) and (f) show the location of one S substitution.

Fermi level. The S atoms are distinguishable as depletions at the location of Se atoms of the topmost  $1T$ -TiSe $_2$  layer with S concentrations  $x = 0.14 \pm 0.02$  for Fig. 1(a) and  $x = 0.34 \pm 0.01$  for Fig. 1(b), determined with statistics made on several similar images. Well-known native defects are also present in negligible quantities [31], including iodine and oxygen substitutions, as well as selenium vacancies which appear as depletions too. The distinction between S substitutions and Se vacancies is clear as shown by the line profile in the inset of Fig. 1(a). Regardless of the applied  $V_{\text{bias}}$ , S substitutions always appear as depletions with a  $z$  value of about 14 pm lower than the Se value, which corresponds to the difference of ionic radius sizes between ions  $\text{S}^{2-}$  and  $\text{Se}^{2-}$  [see the red arrow in the inset of Fig. 1(a)]. The electronegativity difference between S and Se being indeed very small, the S atom fingerprint is essentially topographic. The average radial distribution function  $g(r)$  [32],

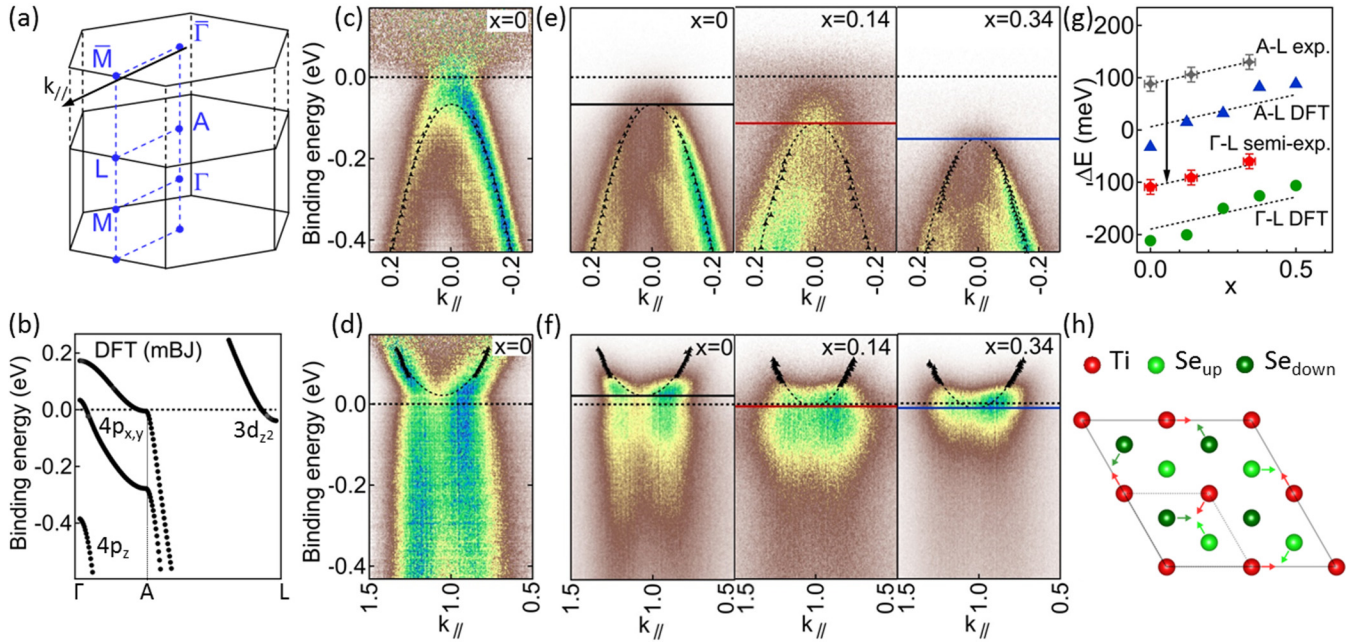


FIG. 2. (a)  $1T$ - $\text{TiSe}_2$  bulk and surface Brillouin zones. (b) DFT electronic band structure along the  $\Gamma$ - $A$ - $L$  path in the normal phase. (c) and (d) RT momentum distribution curve- (MDC-) normalized ARPES spectra of pristine  $1T$ - $\text{TiSe}_2$  at the  $\bar{\Gamma}$  and  $\bar{M}$  points of the surface BZ, respectively. (e) ARPES spectra of  $1T$ - $\text{TiSe}_{2-x}\text{S}_x$  crystals for  $x = 0, 0.14$ , and  $0.34$  (from left to right) displaying the valence band at  $\bar{\Gamma}$ . (f) RT ARPES spectra of the conduction band recorded at  $\bar{M}$  as a function of  $x$  (from left to right). (g)  $A$ - $L$  gap and  $\Gamma$ - $L$  overlap values obtained from DFT simulations and ARPES measurements at room temperature as a function of the sulfur concentration  $x$ . The  $\Gamma$ - $L$  experimental values (red markers) are obtained by shifting the experimental  $A$ - $L$  values (in gray) by the energy difference in DFT between the top of the hole pockets at  $\Gamma$  and  $A$  as illustrated by the black arrow. Negative and positive values, respectively, refer to  $e$ - $h$  band overlap and band gap. (h) Top view of the  $1T$ - $\text{TiSe}_2$  structure and lattice deformation associated with the CDW.

calculated for many different central S atoms, is displayed in the inset of Fig. 1(b) and shows that S atoms are randomly distributed.

Figures 1(c) and 1(d) display STM images of the same zones as Figs. 1(a) and 1(b) with  $V_{\text{bias}} = +0.15$  V in order to highlight the commensurate CDW charge modulation. Whereas low concentrations of intercalated-Ti atoms significantly affect the long-range phase coherence of the CDW [11], no phase shift was observed on these two S-substituted samples at low temperatures. The phase coherence of the charge modulation is thus totally insensitive to S substitutions with concentrations at least up to  $x = 0.34$ . Figures 1(e) and 1(f) compare DFT-simulated STM images with  $V_{\text{bias}} = +0.6$  V (e) and  $V_{\text{bias}} = +0.1$  V (f) and measured STM images with  $V_{\text{bias}} = +0.6$  V (e) and  $V_{\text{bias}} = +0.15$  V (f). Figure 1(e) confirms the S substitution identification at  $V_{\text{bias}} = +0.6$  V. Also, even if at lower  $V_{\text{bias}}$  the CDW modulation tends to hide the topographic depletions associated with S substitutions of nondisplaced Se atoms of the PLD [11], it is still possible to identify them as weakened CDW maxima [see black arrows in Fig. 1(f)].

Let us now focus on the  $x$  dependence of the  $1T$ - $\text{TiSe}_2$  band structure. The  $1T$ - $\text{TiSe}_2$  low-energy electronic states consist of a Se  $4p$  hole pocket and Ti  $3d$  electron pockets at the  $\Gamma$  and three-equivalent  $L$  points of the three-dimensional (3D) Brillouin zone (BZ) [see Fig. 2(a)]. The DFT-calculated hole pocket is composed of two weakly dispersing  $p_{x,y}$  bands along  $\Gamma$ - $A$  and one strongly dispersing band of mainly  $p_z$

character at higher binding energy [33], whereas the Ti  $3d$  electron-pocket is of mainly  $d_{z^2}$  character [see Fig. 2(b)].

Figures 2(c) and 2(d) show RT ARPES spectra at the  $\bar{\Gamma}$  and  $\bar{M}$  points of the hexagonal surface BZ [see Fig. 2(a)] of pristine  $1T$ - $\text{TiSe}_2$  normalized according to MDCs for a better visualization of the electron and hole band dispersions. These (black dashed curves) are obtained by Lorentzian fitting of MDCs [black markers on (c) and (d)] throughout our ARPES study. Since He-I ARPES is mainly probing the  $A$ - $L$  plane of the 3D BZ (in a free-electron final-state picture) [34], only the Se  $4p_{x,y}$  bands are seen in our  $\bar{\Gamma}$  ARPES spectra in Fig. 2(e). Whereas the binding energy of the Se  $4p$  band (indicated by horizontal lines) strongly increases with  $x$ , the bottom of the Ti  $3d$  electron band at  $\bar{M}$  is only slightly shifted [Fig. 2(f)]. Thus, in contrast to the electron-donors Ti and Cu intercalants that shift the  $1T$ - $\text{TiSe}_2$  chemical potential [19,20], isovalent S substitutions change the RT  $e$ - $h$  band overlap.

More precisely, the experimental  $\bar{\Gamma}$ - $\bar{M}$  band gap is found to linearly increase with  $x$  [ $A$ - $L$  experimental in Fig. 2(g)] with a slope in very good agreement with those of both the DFT-calculated  $A$ - $L$  band gap and the  $\Gamma$ - $L$  band overlap variations [blue and green markers in Fig. 2(g), respectively]. This indicates first, that the DFT-calculated  $k_z$  dispersion along  $\Gamma$ - $A$  remains rather insensitive to S substitutions. Second, to obtain a *semiempirical* S-concentration dependence of the  $\Gamma$ - $L$  band overlap, we consider that DFT well reproduces the experimental  $k_z$  dispersion along  $\Gamma$ - $A$ , and we shift the experimental  $\bar{\Gamma}$ - $\bar{M}$  values by the energy difference in DFT

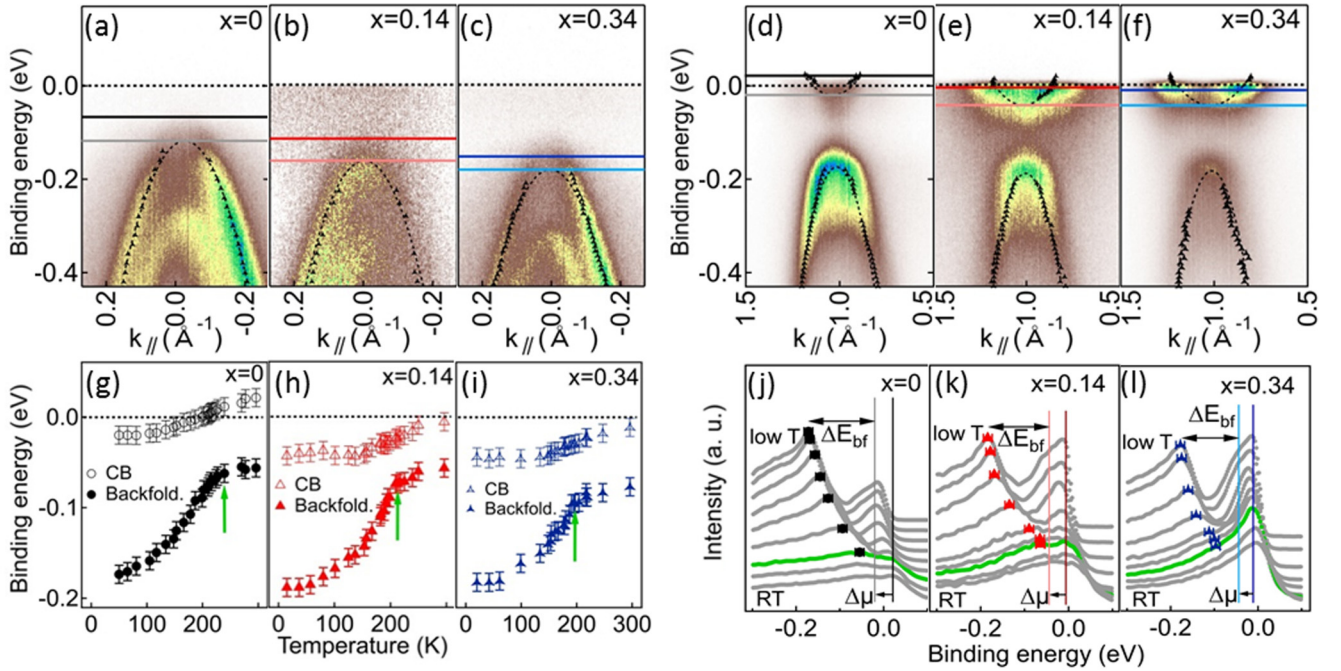


FIG. 3. (a)–(c) ARPES spectra of  $1T\text{-TiSe}_{2-x}\text{S}_x$  for  $x = 0, 0.14$ , and  $0.34$  recorded at low temperatures ( $T = 46 \pm 5$  K) and displaying the valence band at  $\bar{\Gamma}$ . (d)–(f) Low-temperature ARPES spectra measured at  $\bar{M}$  where the backfolded band is well visible. The two lines on each spectrum (a)–(f) indicate the determined valence- and conduction-band extrema at room (upper lines) and low (lower lines) temperatures. (g)–(i) Evolution of the conduction-band minimum and the backfolded weight maximum as a function of the temperature for the three crystals. (j)–(l) energy distribution curves (EDCs) taken on spectra at  $\bar{M}$  as a function of temperature for  $x = 0, 0.14$ , and  $0.34$ . The markers indicate the position of the backfolded spectral weight maximum, and the green EDCs correspond to the maximum temperature at which it can still be identified [the corresponding extracted positions on (g)–(i) are indicated by the green arrows].

between the top of the hole pocket at  $\Gamma$  and  $A$  [red markers and arrow in Fig. 2(g)].

At low temperatures, in the CDW phase, the  $\Gamma$  and  $L$  points are connected by the new reciprocal lattice vectors corresponding to the doubling of the lattice periodicity and large band renormalizations at high-symmetry points of the BZ as well as a large transfer of spectral weight to backfolded bands appear in ARPES. The  $p$ - $d$  hybridization is strongly orbital and  $k_z$  dependent [35] and mainly leads to the renormalization of the Se  $4p$  bands at  $\Gamma$  and Ti  $3d$  bands at  $L$  that derive from the atoms involved in the Ti-Se bond shortening of the PLD [Fig. 2(h)].

ARPES spectra at  $\bar{\Gamma}$  in the CDW phase are displayed in Figs. 3(a)–3(c) for  $x = 0, 0.14$ , and  $0.34$ , respectively, and show Se  $4p$  bands that have shifted to higher binding energy upon temperature lowering [see the two horizontal lines Figs. 3(a)–3(c)]. These shifts are mainly associated with the temperature-induced chemical-potential shift  $\Delta\mu(T)$  arising from the effect of the Fermi-Dirac cutoff on the overlapped hole and electron bands with nonequal band masses [36]. Focusing on the  $x$ -dependent evolutions of both the Se  $4p$  backfolded band and the Ti  $3d$  electron pocket at  $\bar{M}$  in the CDW state [Figs. 3(d)–3(f)], we first recognize the characteristic backfolded Se  $4p$  bands coming from  $\Gamma$  for all three samples with yet a diminished spectral weight for  $x = 0.34$ . Then, we also observe slight shifts of the electron pocket minimum with respect to the RT ARPES spectra. The electron pocket minimum is not influenced by the CDW transition since the lowest Ti  $3d$  conduction band in the CDW phase

derives from Ti atoms that do not move with the PLD [37] [Fig. 2(h)]. In fact, the observed energy shift of the electron pocket minimum also fully relates to  $\Delta\mu(T)$ . It therefore depends on the RT  $e$ - $h$  band overlap as exemplified by the decreasing  $\Delta\mu$  values of  $\sim 41$ ,  $\sim 38$ , and  $\sim 33$  meV for  $x = 0, 0.14$  and  $0.34$ , respectively, obtained for the energy shift of the Ti  $3d$  bands from room to low temperatures [as indicated by the two horizontal lines Figs. 3(d)–3(f)].

The detailed  $T$  evolution of the Ti  $3d$  conduction and Se  $4p$  backfolded bands extrema of our three  $1T\text{-TiSe}_{2-x}\text{S}_x$  crystals are indicated in Figs. 3(g)–3(i). They have been obtained from parabolic fits [dashed lines Figs. 3(d)–3(f)] of the MDC maxima determined on the ARPES data as for the RT case [black symbols Figs. 3(d)–3(f)]. The effective masses have been kept fixed at the high-temperature values for all temperatures. For the backfolded band, the maxima positions are adjusted to the maxima of the EDCs taken exactly at  $\bar{M}$  as shown in Figs. 3(j)–3(l). We see the downward shift of the Se  $4p$  backfolded bands accompanied by continuous increases in their spectral weight. The green curves are EDCs obtained at the maximum temperature at which the backfolding spectral weight can be straightforwardly identified, i.e., approximately at the critical CDW temperatures [the corresponding Se  $4p$  backfolded band positions are indicated by the green arrows in Figs. 3(g)–3(i)].

Within a BCS-like approach [36,38], the shift of the backfolded band at  $L$  [corrected by  $\Delta\mu(T)$ ] relates to the order parameter  $\Delta$  describing the coupling strength between the valence band at  $\Gamma$  and the three-symmetry equivalent conduction

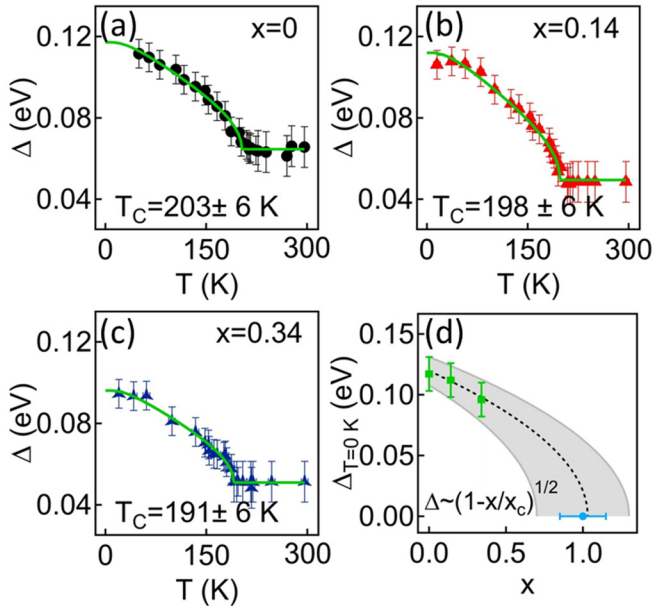


FIG. 4. (a)–(c)  $T$  dependence of the CDW order parameter  $\Delta$  deduced from ARPES for  $x = 0, 0.14$ , and  $0.34$ , respectively. For each sample,  $\Delta(T)$  is fitted with a BCS-like power law given by  $\Delta(T) \propto \tanh(A\sqrt{T_c/T-1}) + \Delta(T_c)$ , where  $A = 0.9$  is a proportional constant. (d)  $x$  dependence of the order parameter at  $T = 0$  K,  $\Delta(0)$ . The black dashed line is a mean-field-like fit of  $\Delta$  vs  $x$  given by  $\Delta/\Delta_{x=0} = (1 - x/x_c)^{1/2}$ , based only on the three  $\Delta_{x=0}$  values extracted from (a)–(c). The shaded area displays the possible range of values obtained from the upper and lower fits. In (d), the blue dot is excluded from the fit and indicates that the  $2 \times 2$  charge modulation is not observed with STM measurements for  $x \approx 1$ .

bands at  $L$  as  $\Delta(T) = \{\Delta E_{bf}(T) \times [\Delta E_{bf}(T) - E_g]\}^{1/2}/\sqrt{3}$ , where  $\Delta E_{bf}(T)$  is the shift of the backfolded band and  $E_g$  is the  $e$ - $h$  band overlap (between  $\Gamma$  and  $L$ ) in the normal phase [36,38]. Figures 4(a)–4(c) show the  $T$  dependence of the order parameter  $\Delta$  calculated with  $\Delta E_{bf}(T)$  obtained from ARPES and using our semiempirical values of the  $e$ - $h$  band overlap  $E_g$ . Note that the finite value of the order parameter for  $T > T_c$  is due to a CDW-fluctuation regime above  $T_c$  known to occur for  $1T$ -TiSe<sub>2</sub> [39]. Using a BCS gap equation to fit the  $\Delta$  values,  $\Delta(T) \propto \tanh(A\sqrt{T_c/T-1}) + \Delta(T_c)$  [40], we obtain  $T_c$  values of  $203 \pm 6$ ,  $198 \pm 6$ , and  $191 \pm 6$  K for  $x = 0, 0.14 \pm 0.02$ , and  $0.34 \pm 0.01$ , respectively, again demonstrating that the CDW phase transition is rather stable against S substitutions in that range of concentrations. According to Ref. [41], the electronic instability is mainly related to the density of states at the point of band intersection in the folded zone and less to the number of carriers in each pocket. Since substituting sulfur in  $1T$ -TiSe<sub>2</sub> essentially changes the overlap between the electron and the hole pockets, a rather small variation of  $T_c$  is expected. Nevertheless, our ARPES measurements also reveal a slow but continuous decrease in the order parameter at  $T = 0$  K,  $\Delta(0)$  [ $0.117 \pm 0.014$ ,  $0.112 \pm 0.014$ , and  $0.96 \pm 0.014$  eV for  $x = 0, 0.14 \pm 0.02$ , and  $0.34 \pm 0.02$ , respectively]. Focusing on the  $x$  dependence of  $\Delta(0)$ , Fig. 4(d), the first three points are fitted considering a mean-field-like scaling behavior. We anticipate a complete suppression of the CDW phase transition

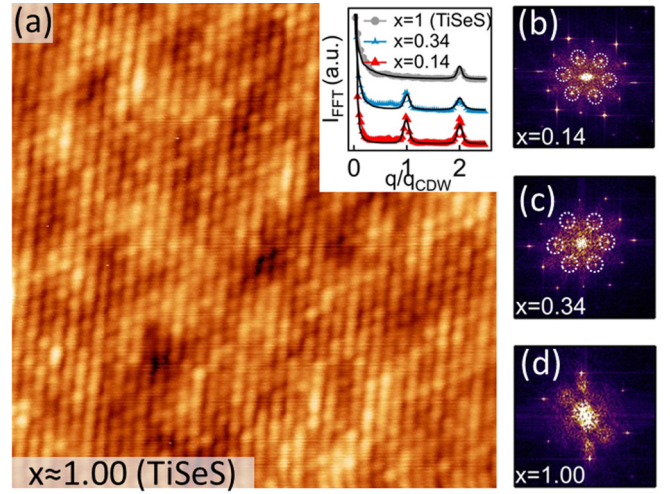


FIG. 5. (a) Constant current ( $I = 0.10$  nA) STM image of  $1T$ -TiSe<sub>2-x</sub>S<sub>x</sub> with  $x \approx 1$  recorded at  $T = 4.5$  K with applied bias voltage  $V_{\text{bias}} = +0.05$  V ( $11 \times 11$  nm<sup>2</sup>). The inset shows line profiles of fast-Fourier-transform (FFT) spots taken on the FFT-amplitude plots (b)–(d) obtained from STM images of the  $11T$ -TiSe<sub>2-x</sub>S<sub>x</sub> crystals in Figs. 1(c) and 1(d) for  $x = 0.14, 0.34$ , and in Fig. 5(a) for  $x \approx 1$ , respectively. The white circles show the extra spots originating from the CDW. For  $x \approx 1$ , the extra spots coming from the  $2 \times 2$  charge modulation are not present.

at a critical sulfur concentration  $x_c$  between 0.7 and 1.3, which is in good agreement with the critical value given in Ref. [5].

As a confirmation, we show, in Fig. 5, LT-STM results obtained on a S-substituted  $1T$ -TiSe<sub>2</sub> crystal with  $x \approx 1$  and negligible intercalated-Ti concentration. With  $V_{\text{bias}} = +0.05$  V, the CDW modulation at 4.5 K is not distinguishable. Comparing line profiles of the  $(2 \times 2)$  and  $(1 \times 1)$  FFT spots for  $x = 0.14, 0.34$ , and 1 [inset in Fig. 5(a)], taken in Figs. 5(b)–5(d), respectively, we see that the peak at  $q = q_{cdw}$  corresponding to the  $2 \times 2$  charge modulation is well visible for  $x = 0.14$  and  $x = 0.34$  but does not exist for  $x \approx 1$ , demonstrating that for this sulfur concentration (corresponding to  $x_c$  deduced from ARPES data), the CDW transition is removed.

At this stage, we have shown that slight S substitutions induce a slow but continuous increase (decrease) of the  $e$ - $h$  band gap (overlap) of the semimetallic normal state, well reproduced by DFT and that the CDW disappears at a rather high  $x_c$ . We now show that the reductions of both CDW order parameters  $\Delta$  and  $T_c$  are intimately related to the  $e$ - $h$  band-gap opening. Figure 6 displays the DFT-calculated energy difference between the electron band minimum at  $L$  and the hole band maximum at  $\Gamma(E_g)$  as a function of  $x$  shifted to match our ARPES-extracted semiempirical values [green markers, see also Fig. 2(g)]. Interestingly, extrapolating the linear dependence of  $E_g$  with  $x$  to higher substitutions, a semimetal-to-semiconductor transition ( $E_g = 0$ ) of the normal state is expected at a critical S concentration of  $0.65 \pm 0.15$ , a value close to those proposed in previous temperature-dependent resistivity and Raman-scattering measurements [5,15–18] and to the concentration  $x_c$  at which the CDW is suppressed.

At last, our DFT analysis reveals the underlying mechanisms responsible for the  $e$ - $h$  band-gap opening and the

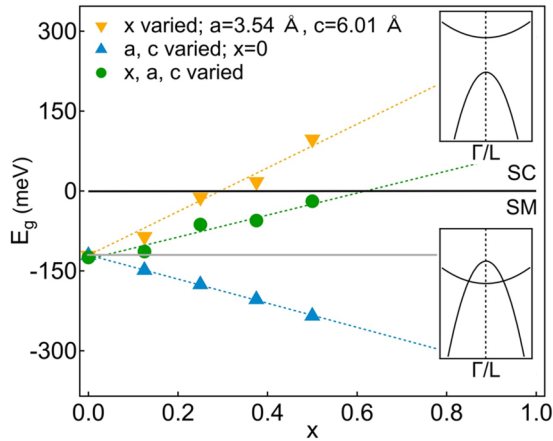


FIG. 6. Energy difference between the electron band minimum at  $L$  and the hole band maximum at  $\Gamma$  ( $E_g$ ) as obtained by DFT for  $x = 0, 0.125, 0.25, 0.375, \text{ and } 0.5$  and lattice parameters  $a$  and  $c$  fixed at their experimental values taken from [16] (green circles).  $E_g < 0$  and  $E_g > 0$ , respectively, refer to semimetallic and semiconducting normal state. The  $E_g$  values obtained by substituting S atoms in the DFT superstructure but keeping  $a = 3.54$  and  $c = 6.01$  Å fixed are displayed by the orange triangles. Inversely, the  $E_g$  values corresponding to  $x = 0$  but decreasing lattice parameters  $a$  and  $c$  are depicted by the blue triangles. The dashed lines are linear fits to the  $E_g$  values that have been all shifted to match our ARPES-extracted values.

CDW suppression. We first mimic chemical pressure effects introduced by isovalent S substitutions by calculating the electronic band structures of  $1T$ -TiSe<sub>2</sub> for couples of  $a$  and  $c$  lattice parameters corresponding to the experimental values of Ref. [16]. As can be seen in Fig. 6 (blue markers), the overlap of the Ti  $3d$  electron and the Se  $4p$  hole bands linearly increases when the lattice contracts as expected from positive chemical pressure effects. On the other hand, keeping fixed the lattice parameters to their pristine values while varying

only the S content, leads to computed  $E_g$  that evolves almost linearly with  $x$  towards a semiconducting band configuration (orange triangles, Fig. 6). Indeed, substituting the Se  $4p$  orbitals by the more localized S  $3p$  ones strengthens the ionic character of the ionocovalent transition-metal-chalcogen bonds, therefore acting as a charge localization effect and leading to a reduced  $p$ - $d$  hybridization. Overall, as seen in Fig. 6, charge localization dominates the chemical pressure effect and therefore drives the  $e$ - $h$  band gap opening, i.e. the CDW suppression.

## V. CONCLUSION

To summarize, we have investigated the CDW suppression in well-characterized  $1T$ -TiSe<sub>2-x</sub>S<sub>x</sub> single crystals by means of ARPES, STM, and DFT calculations. We have demonstrated that isovalent S substitutions reduce the  $e$ - $h$  band overlap in the normal state and do not affect the long-range phase coherent CDW state as long as the  $1T$ -TiSe<sub>2</sub> normal state remains semimetallic. The CDW has been experimentally found to be suppressed for  $x \geq 0.7$  in good agreement with the DFT-predicted semimetal-to-semiconductor transition. Our DFT analysis has revealed that, whereas the isovalent S substitution induces an increase in the overlap of the Ti  $3d$  electron and the Se  $4p$  hole bands by positive chemical pressure, charge localization effects lead to a reduced  $p$ - $d$  hybridization and dominates the  $e$ - $h$  band gap opening. The mechanism of the CDW suppression in  $1T$ -TiSe<sub>2-x</sub>S<sub>x</sub> therefore indicates that only a semimetallic normal-state Fermi surface is unstable towards the  $2 \times 2 \times 2$  CDW phase.

## ACKNOWLEDGMENTS

This project was supported by the Fonds National Suisse pour la Recherche Scientifique through Division II. E.R. acknowledges support from the Swiss National Science Foundation (SNSF) Grant No. P300P2-164649. Skillful technical assistance was provided by F. Bourqui, B. Hediger, and O. Raetz.

- [1] Q. H. Wang, K. Kalantar-Zadeh, A. Kis, J. N. Coleman, and M. S. Strano, *Nat. Nanotechnol.* **7**, 699 (2012).
- [2] K. Rossnagel, *J. Phys.: Condens. Matter* **23**, 213001 (2011).
- [3] A. H. Castro Neto, *Phys. Rev. Lett.* **86**, 4382 (2001).
- [4] H. Wang, H. Yuan, S. Sae Hong, Y. Li, and Y. Cui, *Chem. Soc. Rev.* **44**, 2664 (2015).
- [5] F. Di Salvo, D. Moncton, and J. Waszczak, *Phys. Rev. B* **14**, 4321 (1976).
- [6] B. Hildebrand, T. Jaouen, M.-L. Mottas, G. Monney, C. Barreateau, E. Giannini, D. R. Bowler, and P. Aebi, *Phys. Rev. Lett.* **120**, 136404 (2018).
- [7] L. J. Li, E. C. T. O'Farrell, K. P. Loh, G. Eda, B. Özyilmaz, and A. H. Castro Neto, *Nature (London)* **529**, 185 (2015).
- [8] E. Morosan, H. W. Zandbergen, B. S. Dennis, J. W. G. Bos, Y. Onose, T. Klimczuk, A. P. Ramirez, N. P. Ong, and R. J. Cava, *Nat. Phys.* **2**, 544 (2006).
- [9] A. F. Kusmartseva, B. Sipos, H. Berger, L. Forró, and E. Tutiš, *Phys. Rev. Lett.* **103**, 236401 (2009).
- [10] B. Hildebrand, T. Jaouen, C. Didiot, E. Razzoli, G. Monney, M.-L. Mottas, A. Ubaldini, H. Berger, C. Barreateau, H. Beck, D. R. Bowler, and P. Aebi, *Phys. Rev. B* **93**, 125140 (2016).
- [11] B. Hildebrand, T. Jaouen, C. Didiot, E. Razzoli, G. Monney, M.-L. Mottas, F. Vanini, C. Barreateau, A. Ubaldini, E. Giannini, H. Berger, D. R. Bowler, and P. Aebi, *Phys. Rev. B* **95**, 081104(R) (2017).
- [12] C. H. Chen, W. Fabian, F. C. Brown, K. C. Woo, B. Davies, B. DeLong, and A. H. Thompson, *Phys. Rev. B* **21**, 615 (1980).
- [13] H. Isomaki and J. von Boehm, *J. Phys. C* **14**, L75 (1981).
- [14] C. Wang, C. G. Slough, and R. V. Coleman, *J. Vac. Sci. Technol. B* **9**, 1048 (1991).
- [15] J. M. Lopez-Castillo, A. Amara, S. Jandl, J.-P. Jay-Gerin, C. Ayache, and M. J. Aubin, *Phys. Rev. B* **36**, 4249 (1987).
- [16] Y. Miyahara, H. Bando, and H. Ozaki, *J. Phys.: Condens. Matter* **8**, 7453 (1996).
- [17] M. M. May, C. Brabetz, C. Janowitz, and R. Manzke, *Phys. Rev. Lett.* **107**, 176405 (2011).

- [18] G. A. Freund and R. D. Kirby, *Phys. Rev. B* **30**, 7122 (1984).
- [19] T. Jaouen, B. Hildebrand, M.-L. Mottas, M. Di Giovannantonio, P. Ruffieux, M. Rumo, C. W. Nicholson, E. Razzoli, C. Barreteau, A. Ubaldini, E. Giannini, F. Vanini, H. Beck, C. Monney, and P. Aebi, [arXiv:1812.00906](https://arxiv.org/abs/1812.00906).
- [20] D. Qian, D. Hsieh, L. Wray, E. Morosan, N. L. Wang, Y. Xia, R. J. Cava, and M. Z. Hasan, *Phys. Rev. Lett.* **98**, 117007 (2007).
- [21] G. Kresse and J. Hafner, *Phys. Rev. B* **47**, 558 (1993).
- [22] G. Kresse and J. Furthmüller, *Phys. Rev. B* **54**, 11169 (1996).
- [23] G. Kresse and D. Joubert, *Phys. Rev. B* **59**, 1758 (1999).
- [24] J. P. Perdew, K. Burke, and M. Ernzerhof, *Phys. Rev. Lett.* **77**, 3865 (1996).
- [25] J. Tersoff and D. R. Hamann, *Phys. Rev. Lett.* **50**, 1998 (1983).
- [26] W. A. Hofer, *Prog. Surf. Sci.*, **71**, 147 (2003).
- [27] P. Blaha, K. Schwarz, G. K. H. Madsen, D. Kvasnicka, and J. Luitz, *WIEN2K, An Augmented Plane Wave + Local Orbitals Program for Calculating Crystal Properties* (Karlheinz Schwarz, Technical Universität Wien, Austria, 2001).
- [28] F. Tran and P. Blaha, *Phys. Rev. Lett.* **102**, 226401 (2009).
- [29] D. Koller, F. Tran, and P. Blaha, *Phys. Rev. B* **85**, 155109 (2012).
- [30] O. Rubel, A. Bokhanchuk, S. J. Ahmed, and E. Assmann, *Phys. Rev. B* **90**, 115202 (2014).
- [31] B. Hildebrand, C. Didiot, A. M. Novello, G. Monney, A. Scarfato, A. Ubaldini, H. Berger, D. R. Bowler, C. Renner, and P. Aebi, *Phys. Rev. Lett.* **112**, 197001 (2014).
- [32] P. M. Chaikin and T. C. Lubensky, *Principles of Condensed Matter Physics* (Cambridge University Press, Cambridge, UK, 1995).
- [33] Z. Vydrova, E. F. Schwier, G. Monney, T. Jaouen, E. Razzoli, C. Monney, B. Hildebrand, C. Didiot, H. Berger, T. Schmitt, V. N. Strocov, F. Vanini, and P. Aebi, *Phys. Rev. B* **91**, 235129 (2015).
- [34] T. Pillo, J. Hayoz, H. Berger, F. Lévy, L. Schlapbach, and P. Aebi, *Phys. Rev. B* **61**, 16213 (2000).
- [35] M. D. Watson, O. J. Clark, F. Mazzola, I. Marković, V. Sunko, T. K. Kim, K. Rossnagel, and P. D. C. King, *Phys. Rev. Lett.* **122**, 076404 (2019).
- [36] C. Monney, H. Cercellier, F. Clerc, C. Battaglia, E. F. Schwier, C. Didiot, M. G. Garnier, H. Beck, P. Aebi, H. Berger, L. Forró, and L. Patthey, *Phys. Rev. B* **79**, 045116 (2009).
- [37] M. Hellgren, J. Baima, R. Bianco, M. Calandra, F. Mauri, and L. Wirtz, *Phys. Rev. Lett.* **119**, 176401 (2017).
- [38] C. Monney, E. F. Schwier, M. G. Garnier, N. Mariotti, C. Didiot, H. Beck, P. Aebi, H. Cercellier, J. Marcus, C. Battaglia, H. Berger, and A. N. Titov, *Phys. Rev. B* **81**, 155104 (2010).
- [39] C. Monney, G. Monney, P. Aebi, and H. Beck, *Phys. Rev. B* **85**, 235150 (2012).
- [40] P. Chen, Y.-H. Chan, X.-Y. Fang, Y. Zhang, M. Y. Chou, S.-K. Mo, Z. Hussain, A.-V. Fedorov, and T. C. Chiang, *Nat. Commun.* **6**, 8943 (2015).
- [41] C. Chen, B. Singh, H. Lin, and V. M. Pereira, *Phys. Rev. Lett.* **121**, 226602 (2018).